

# Sol–gel derived mesoporous Pt and Cr-doped WO<sub>3</sub> thin films: the role played by mesoporosity and metal doping in enhancing the gas sensing properties

Massimiliano D'Arienzo · Maurizio Crippa · Paolo Gentile ·  
Claudio Maria Mari · Stefano Polizzi · Riccardo Ruffo ·  
Roberto Scotti · Laura Wahba · Franca Morazzoni

Received: 21 February 2011 / Accepted: 16 August 2011 / Published online: 8 September 2011  
© Springer Science+Business Media, LLC 2011

**Abstract** Mesoporous Cr or Pt-doped WO<sub>3</sub> thin films to be employed as ammonia gas sensors were prepared by a fast one-step sol–gel procedure, based on the use of triblock copolymer as templating agent. The obtained films were constituted by aggregates of interconnected WO<sub>3</sub> nanocrystals (20–50 nm) separated by mesopores with dimensions ranging between 2 and 15 nm. The doping metals, Pt and Cr, resulted differently hosted in the WO<sub>3</sub> mesoporous matrix. Chromium is homogeneously dispersed in the oxide matrix, mainly as Cr(III) and Cr(V) centers, as revealed by EPR spectroscopy; instead platinum segregated as Pt (0) nanoparticles (4 nm) mainly included inside the WO<sub>3</sub> nanocrystals. The semiconductor layers containing Pt nanoclusters revealed, upon exposure to NH<sub>3</sub>, remarkable electrical responses, much higher than Cr-doped and undoped layers, particularly at low ammonia concentration (6.2 ppm). This behavior was attributed to the presence of Pt nanoparticles segregated inside the

semiconductor matrix, which act as catalysts of the N–H bond cleavage, decreasing the activation barrier in the ammonia dissociation. The role of the mesoporous structure in influencing the chemisorption and the gas diffusion in the WO<sub>3</sub> matrix appeared less decisive than the electronic differences between the two examined doping metals. The overall results suggest that a careful combination between mesoporous architecture and metal doping can really promote the electrical response of WO<sub>3</sub> toward ammonia.

**Keywords** Pt and Cr—doped WO<sub>3</sub> · Mesoporous thin film · Gas sensors · Morphological, electronic and electrical properties

## 1 Introduction

Semiconducting metal oxides have been studied for some decades as sensing materials, in order to detect hazardous gases [1–8]. The mechanism of the metal-oxide sensors is based on the change of electrical conductance in response to the introduction of a small concentration of reducing gas, which reacts with the oxygen species at the oxide surface [1, 4, 5]. Many extensive studies, mainly concerning SnO<sub>2</sub>, widely investigate the dependence of the electrical response on both the electronic and morphological properties of the semiconductor [9–15]. The sensing mechanism towards different gases, H<sub>2</sub> [16], CO [17] and NO<sub>2</sub> [18] was also suggested.

Several mechanistic details were achieved thank to the use of the sol–gel synthetic approach, whose attitude to give nano-materials with very reactive surfaces and controlled particle size and porosity, allows to obtain samples with enhanced electrical response [19–22].

**Electronic supplementary material** The online version of this article (doi:10.1007/s10971-011-2568-7) contains supplementary material, which is available to authorized users.

M. D'Arienzo (✉) · M. Crippa · C. M. Mari · R. Ruffo ·  
R. Scotti · L. Wahba · F. Morazzoni  
INSTM, Department of Materials Science, University of Milano-  
Bicocca, Via R. Cozzi 53, 20125 Milan, Italy  
e-mail: massimiliano.darienzo1@unimib.it

P. Gentile  
Department of Geological Sciences and Geotechnologies,  
University of Milano Bicocca, Piazza della Scienza 4,  
20126 Milan, Italy

S. Polizzi  
Department of Molecular Sciences and Nanosystems, Università  
Ca' Foscari Venezia, and INSTM, UdR Venezia, Via Torino  
155/b, 30172 Venezia, Italy

In fact, the performances of semiconductor based sensors are determined by the surface interaction of the oxide with the analyte gas [1–5]. Specifically fast gas diffusion rate through the sensing layer and effective charge transfer between the grains require oxide grain size of nanometric dimensions, comparable to the thickness of the space-charge region [24, 25]. Moreover, high interconnectivity between the particles is needed to facilitate the electronic charge transport [9, 10]; high surface area to favor the gas-oxide interaction and porous structure to improve the gas diffusion throughout the layer [9]. In addition the sensor response can be significantly enhanced by homogeneously dispersing noble metals centres into the oxide matrix, such as Pt, Pd, Ag, which act as catalysts of the chemical interaction between gas molecules and the semiconductor [11, 15].

In this frame, our group prepared nanostructured thin films of transition metal doped  $\text{SnO}_2$  by the sol–gel method and demonstrated the improving effect of the particle nanosize and of the homogeneously dispersed doping metal on the oxide sensing properties [11, 15]. The dependence of electrical response on the film morphology, on the oxidation state of the metals, as well as the electron transfer at the interface gas/metal/oxide were also investigated. The metal and oxygen defects responsible for the variations in the semiconductor resistance were revealed by electron spin resonance measurements [11, 18].

Moreover, in order to better detail the effect of the porous structure on the oxide sensing properties, three dimensionally ordered macroporous materials (3DOM), specifically Pt-doped  $\text{SnO}_2$  inverted opal films, were synthesized by alkoxide-based sol–gel processes [10, 11]. The self assembled ordered array of colloidal polymeric microspheres was used as the template; the interstices were filled with metal alkoxide solution, then hydrolyzed and densified. The obtained inverted opal architecture is constituted of macropores connected through holes, resulting from the contact between the template spheres, surrounded by strongly interconnected nanocrystalline particles. These morphological features guarantee high surface chemisorption and easy gas diffusion. Recently, our group proposed an innovative one-step sol–gel preparation of Pt doped  $\text{SnO}_2$  as inverse opal thin films by dip-coating deposition, to easily obtain three dimensional ordered macroporous metal oxides with high surface area and homogeneous dopant metal distribution. The procedure enables the self-assembled formation of closely-packed PS template array and the simultaneous infiltration of the precursors into the voids of the structure, making it possible to obtain the oxide solid skeleton around the spheres in one-step [15].

Among semiconductor metal-oxides,  $\text{WO}_3$  has been also considered as one of the most promising materials for toxic gas detection, in particular for ammonia detection [26]. An extensive scientific and engineering research is still active

on this topic, focused on optimizing the sensing properties: electrical response, response rate, gas selectivity and long-term stability [26, 27]. In this context, the tailoring of the morphology and an effective doping method of the oxide matrix still remain important challenges.

We recently studied the behaviour of sol–gel prepared  $\text{WO}_3$  films as  $\text{NH}_3$  sensor and investigated the role Cr, Cu and V dopant, in enhancing the electrical response and in avoiding the resistance overshooting effects observed in undoped  $\text{WO}_3$  [28, 29]. However, the preparation method adopted was relatively time consuming and the sensor performances were evaluated only under high ammonia concentration (500 ppm). Furthermore, no doping with noble metal (such as Pt), which in principle can enhance the  $\text{NH}_3$  dissociation and promotes the response, was carried out.

In this paper, we report a fast and tailored sol–gel one-step procedure to prepare Cr and Pt-doped  $\text{WO}_3$  mesoporous thin films for ammonia gas sensing, based on the use of polyalkyleneoxide triblock copolymer as the templating agent. The purpose was to study the effect of the oxide porous morphology and of the metal homogeneous doping on the sensing properties towards  $\text{NH}_3$ . The morphology of the  $\text{WO}_3$  films and the electronic properties of the doping metal centers were studied by electron microscopy and EPR spectroscopy, in order to suggest a mechanism for the variations of electrical properties in the presence of  $\text{NH}_3$ . Finally the electrical response of the  $\text{WO}_3$  layers was discussed in terms of conductance regime under different gas concentrations, in order to achieve optimum balance between the intensity and the reproducibility of sensor performances. Results supported the validity of the synthesis method here reported to supply promising nanomaterials for the detection of ammonia even at low concentration.

## 2 Experimental section

### 2.1 Chemicals

Poly(alkylene oxide) block copolymer designated  $(\text{HO}(\text{CH}_2\text{CH}_2\text{O})_{20}(\text{CH}_2\text{CH}(\text{CH}_3)\text{O})_{70}(\text{CH}_2\text{CH}_2\text{O})_{20}\text{OH}$  ( $\text{EO}_{20}\text{PO}_{70}\text{EO}_{20}$ ), Pluronic P123); tungsten hexachloride,  $\text{WCl}_6$  99.9%; chromium(III) nitrate nona hydrate  $\text{Cr}(\text{NO}_3)_3 \cdot 9\text{H}_2\text{O}$  99%, bis-(acetylacetonate)platinum(II),  $\text{Pt}(\text{acac})_2$  97% and absolute ethanol (99.9%) were all purchased from Aldrich and used without further purification.

### 2.2 Preparation of precursor suspensions of Pt- and Cr-doped $\text{WO}_3$ sol–gel film and film deposition

The precursor suspensions for the deposition of Pt- and Cr-doped  $\text{WO}_3$  sol–gel films, were prepared according to a

previously reported procedure [23]. The doping was carried out by direct addition of the dopant metal precursor to the reaction solution.

In a typical preparation the copolymer  $\text{EO}_{20}\text{PO}_{70}\text{EO}_{20}$  (1 g) was dissolved in ethanol (10 mL) under magnetic stirring. Then  $\text{WCl}_6$  (400 mg) was added under a  $\text{N}_2$  atmosphere, and the resulting dark blue solution was vigorously stirred for 30 min. Pt (Pt:W molar ratio 0.025) or Cr doping procedure (Cr:W molar ratio 0.025) was carried out by adding the proper amount of  $\text{Pt}(\text{acac})_2$ , or  $\text{Cr}(\text{NO}_3)_3 \cdot 9\text{H}_2\text{O}$ , respectively, to the  $\text{WO}_3$  precursor suspension. The obtained solution was stirred at room temperature in air for 24 h, until the sol phase reached a suitable viscosity ( $\sim 2.5 \pm 0.3$  cSt) for the dip-coating deposition.

Sol-gel films were deposited in air by dip-coating (0.8 cm/min) on Suprasil quartz slides ( $20 \times 20$  mm, 0.25 mm thickness) and dried in air for about 10 min at room temperature. The above cycle was repeated three times, then the film was annealed at 450 °C (heating rate  $2 \text{ }^\circ\text{C min}^{-1}$ ) in air stream ( $80 \text{ cm}^3 \text{ min}^{-1}$ ) for 5 h, in order to fully decompose the polymeric template and all the organic remnants.

Since XRD, BET and EPR analysis of films are difficult to be performed with high accuracy, these characterizations were performed on powders. To gain pure and doped  $\text{WO}_3$  nanopowders, the sol phase used for film deposition was gelled in an open Petri dish at 100 °C in air for 24 h until the xerogel was obtained. This later was calcined under the same conditions used for films in order to completely remove the organics and obtain a green crystalline  $\text{WO}_3$  powder.

### 2.3 Morphological characterization

XRD analysis was performed on  $\text{WO}_3$  powdered samples. X-ray diffraction (XRD) patterns were collected with a Bruker D8 Advance (Cu  $K\alpha$  radiation) in the range  $20\text{--}80^\circ 2\theta$  ( $2\theta$  step  $0.025^\circ$ , count time of 2 s per step).

Specific surface area (SSA) by BET method [28], desorption cumulative pore volume (DCPV) and pore size distribution of micro- and mesopores ( $<50$  nm) by BJH method [29] were measured by nitrogen physisorption using Quantachrome Autosorb-1 apparatus. Cr-doped and Pt-doped  $\text{WO}_3$  powder samples were evacuated at 200 °C for 16 h before the analysis.

Scanning electron microscopy (SEM) measurements of the films were performed by a Vega TS5136 XM Tescan microscope in a high-vacuum configuration. The electron beam excitation was 30 kV at a beam current of 25 pA, and the working distance was 12 mm. In this configuration the beam spot was 38 nm. Prior to SEM analysis, samples were gold-sputtered. The average thickness of sol-gel derived

$\text{WO}_3$  thin films was measured by observing cross-section SEM images of the layers.

High-resolution transmission electron microscopy (HRTEM) and electron diffraction (ED) were performed using a Jeol 3010 apparatus operated at 300 kV with a high-resolution pole piece (0.17 nm point-to-point resolution) and equipped with a Gatan slow-scan 794 CCD camera. Samples were obtained by removing a film portion from the substrates in order to obtain a fine powder sample, then suspended in 2-propanol. A 5  $\mu\text{L}$  drop of this suspension was deposited on a holey carbon film supported on a 3 mm copper grid for TEM investigation.

### 2.4 EPR characterization

The electron paramagnetic resonance (EPR) investigation was performed by a Bruker EMX spectrometer working at the X-band frequency and equipped with an Oxford cryostat operating in the range of temperature 4–298 K.

Cr-doped  $\text{WO}_3$  powders were inserted into quartz glass tubes connected both to a vacuum pumping system and to a controlled gas feed (Synthetic Air).

Spectra were recorded under vacuum conditions ( $10^{-2}$  mbar) at 130 K, on Cr (2%) doped  $\text{WO}_3$  exposed for 60 min to 20 mbar of air at 250 °C, in order to reproduce the conditions of the electrical measurement (see Sect. 2.5).

Modulation frequency was 100 kHz, modulation amplitude 5 gauss, and microwave power 20 mW. The  $g$  values were calculated by standardization with  $\alpha, \alpha'$ -diphenyl- $\beta$ -picryl hydrazyl (DPPH). Care was taken in order to always keep the most sensitive part of the EPR cavity (1 cm length) filled.

### 2.5 Electrical measurements

Suprasil quartz slides were equipped, before film deposition, with two gold current collectors (20 mm) deposited at a distance of about 2 mm from each other by the dc sputtering technique. Then the samples were placed in a quartz chamber sited in an oven, and the measurements were performed at different temperatures, ranging from 200 to 325 °C. The electrical resistance was measured by a programmable electrometer controlled by a PC. To dynamically reproduce environmental conditions in a controlled and reproducible way, a system based on volumetric gas mixing through mass flow controllers and certified bottles was used. The sensing element was initially equilibrated in air flow ( $100 \text{ mL min}^{-1}$ ) at the selected temperature, then  $\text{NH}_3$  (range 6.2–74 ppm)/air mixture was introduced ( $100 \text{ mL min}^{-1}$ ) up to equilibrium conditions. The different gas mixtures were obtained by dilution of the starting  $\text{NH}_3$  (74 ppm)/air mixture using mass flow

controllers. The initial resistance conditions of the film were restored by air equilibration, before again introducing the  $\text{NH}_3/\text{air}$  mixture. The electrical response ( $S$ ) is defined as the ratio between the film resistance under flowing air,  $R_{\text{AIR}}$ , and under flowing  $\text{NH}_3/\text{air}$  mixture,  $R_{\text{MIX}}$ , respectively ( $S = R_{\text{AIR}}/R_{\text{MIX}}$ ).

### 3 Results and discussion

#### 3.1 Structural and morphological characterization

XRD and BET analysis were performed on  $\text{WO}_3$  powdered samples, as the film characterization is difficult to be performed with high accuracy (see Sect. 2).

XRD patterns of Cr-doped  $\text{WO}_3$  powders are shown in Fig. 1. The broadening of the diffraction peaks suggests that the oxide is composed of nanocrystals. The obtained phase can be indexed as monoclinic, in fact the diffractogram shows the (200), (020), and (002) reflections (Fig. 1b) with similar intensities, precisely indicating the type of monoclinic structure (spacegroup:  $P2_1/n$ ,  $a = 0.7297$  nm,  $b = 0.7539$  nm,  $c = 0.7688$  nm,  $\beta = 90.91^\circ$ , JCPDS 43-1035). Identical diffraction patterns were obtained for pure and Pt-doped  $\text{WO}_3$  powders.

Cr and Pt-doped  $\text{WO}_3$  nanopowders resulted mesoporous in the nitrogen physisorption measurements, showing type IV Brunauer isotherm and a broad monomodal pore size distribution centered at 20 nm. As an example, the adsorption–desorption isotherms and the corresponding pore-size distribution of Pt-doped  $\text{WO}_3$  powders are shown in Fig. 2. According to the t-plot (not showed), no micropores were detected. Cr and Pt-doped  $\text{WO}_3$  sol–gel powders exhibit a specific surface area (SSA) of 39.1 and 45.4  $\text{m}^2 \text{g}^{-1}$ ; a DCPV of 0.21 and 0.19  $\text{cm}^3 \text{g}^{-1}$ , respectively.

Scanning electron microscopy (SEM) investigations were performed on both undoped and transition metal-doped  $\text{WO}_3$  films. The average thickness of sol–gel derived

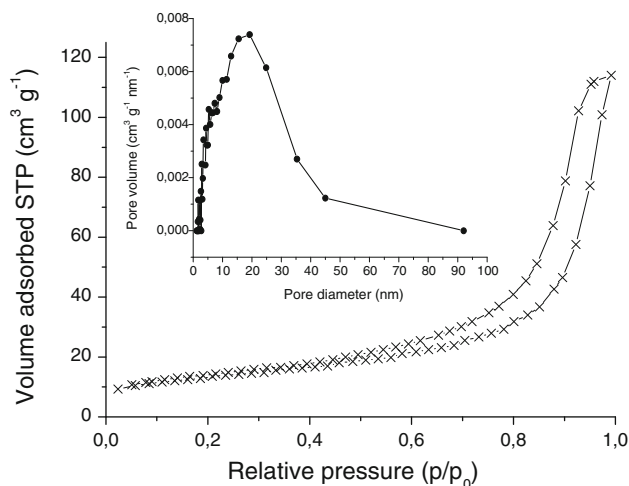
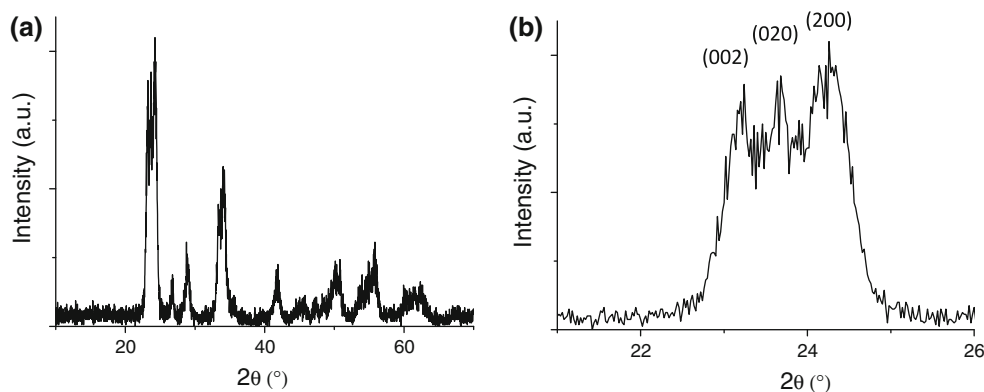


**Fig. 2** Adsorption/desorption isotherm at liquid nitrogen for Pt-doped  $\text{WO}_3$  sol–gel powders. Curves correspond to type IV isotherm with capillary condensation in the mesopores. *Inset* pore size distribution

$\text{WO}_3$  thin films was estimated by observing cross-section images of the layers and resulted in the range of  $540\text{--}620 \pm 15$  nm (see Supporting Information, Fig. S1). Top view SEM micrographs of Pt-doped  $\text{WO}_3$  film (Fig. 3) revealed the presence of porous aggregates of oxide nanoparticles (Fig. 3b). No large cracks were detectable and films with extensive homogeneity were obtained (Fig. 3a). Similar images were obtained for Cr-doped and also for bare  $\text{WO}_3$  films (not shown), confirming that doping by transition metal ions does not affect the film morphology.

TEM images of Pt-doped and Cr-doped  $\text{WO}_3$  sol–gel films are shown in Fig. 3.  $\text{WO}_3$  aggregates are constituted of irregularly shaped interconnected nanocrystals (Fig. 4a, b) with a broad size distribution ranging from 20 to 50 nm, when the statistics is applied to about 150 particles. No amorphous phases and internal defects or pores were detectable. Higher magnification reveals that  $\text{WO}_3$  nanoparticles (Fig. 4c, d) are separated by small

**Fig. 1** **a** X-ray diffraction patterns of Cr-doped  $\text{WO}_3$  sol–gel powders obtained after annealing at 450  $^\circ\text{C}$ . **b** Detail of the diffractogram showing the (200), (020), and (002) reflections of the  $\text{WO}_3$  monoclinic structure



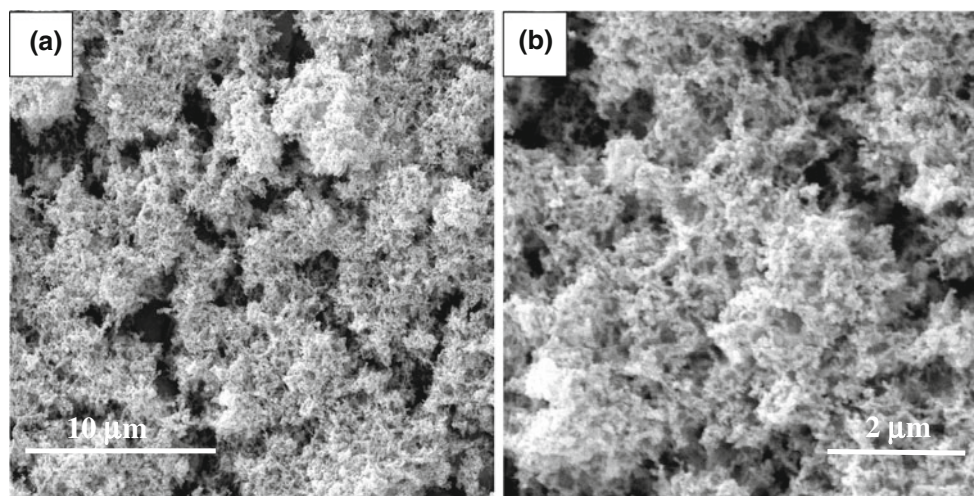


**Fig. 3** SEM micrographs of Pt-doped  $\text{WO}_3$  sol-gel films showing large porous aggregates

mesopores with dimensions ranging between 5 and 15 nm, in agreement with the results obtained by nitrogen physisorption. Unexpectedly, Pt-doped  $\text{WO}_3$  films show well detectable Pt metal nanocrystals; some of those lie at the surface, but the most are included inside the  $\text{WO}_3$  matrix (Fig. 4d). These Pt particles appear to be distributed throughout the whole layer. Conversely, Cr-doped films are exempt of metal particles, suggesting dopant dispersion in the oxide matrix without any evident segregation.

Finally, the selected-area electron diffraction (SAED) patterns collected for Cr-doped and Pt-doped  $\text{WO}_3$  (inset Fig. 4a, b) confirm the monoclinic structure of the oxide nanocrystals already revealed by powder diffraction. TEM analysis performed on undoped  $\text{WO}_3$  sol-gel films gave analogous results (Fig. S2 Supporting Information).

High-resolution (HRTEM) images of Cr-doped (Fig. 4e) and Pt-doped  $\text{WO}_3$  (Fig. 4f) samples evidence that the lattice fringes of the nanocrystals have a spacing of 3.79 Å, which reasonably matches the interplanar distance of the (200) plane of the monoclinic tungsten trioxide (ICDD 71-0131).

Inset in Fig. 4f provides insight into the structure of the spherical Pt metal nanoparticles observed in Pt-doped samples (Fig. 4d, f). Pt particles have diameter of about 4 nm and calculated interplanar spacing of 2.25 Å (not shown), in agreement with the (111) crystallographic plane of Pt (JCPDS 04-0802).

It appears that Pt ions of the precursor solution are reduced within the  $\text{WO}_3$  lattice, at variance with Cr ions, as expected, and aggregate into clusters, probably favoured by the possibility of moving through the channels of the  $\text{WO}_3$  perovskite open structure.

### 3.2 EPR investigation

While zerovalent Pt was easily detectable by the presence of metal nanoparticles, no information about the electronic states of Cr centers became evident.

Considering that Cr centers can in principle give rise to paramagnetic electronic states, an Electron Paramagnetic Resonance (EPR) investigation was performed on Cr-doped  $\text{WO}_3$  powders, after exposure to 20 mbar of synthetic air at 250 °C, this condition simulating the operative sensor temperature (see the next section).

Figure 5 shows the spectra recorded at 130 K after sample evacuation ( $10^{-2}$  mbar). The resonance lines are similar to those previously reported by us for differently prepared Cr-doped  $\text{WO}_3$  samples and attributed to  $\beta$  Cr species ( $\text{Cr}_2\text{O}_3$  like centers),  $\delta$  Cr species (tetragonally distorted Cr(III) centers),  $\gamma$  Cr species (Cr(V) centers) [30, 31]. The total amount of paramagnetic centers is about 14% of the nominal Cr content (2%) and assesses that a significant part of chromium is in an oxidized paramagnetic electronic state.

### 3.3 Electrical measurements

$\text{WO}_3$  is a n-type semiconductor oxide, whose resistance decreases under  $\text{NH}_3$  and increases under air. Its electrical response to  $\text{NH}_3$  is associated with specific reactions at the gas-oxide interface. In previous works we suggested that, in the first stage of the reaction, ammonia molecules chemisorb on the Lewis and Brønsted acidic sites of  $\text{WO}_3$  surface and undergo dehydrogenation through the capture of hydrogen atoms by the oxygen lattice centers ( $\text{O}_\text{O}$ ) [28, 29]. Hydroxyl

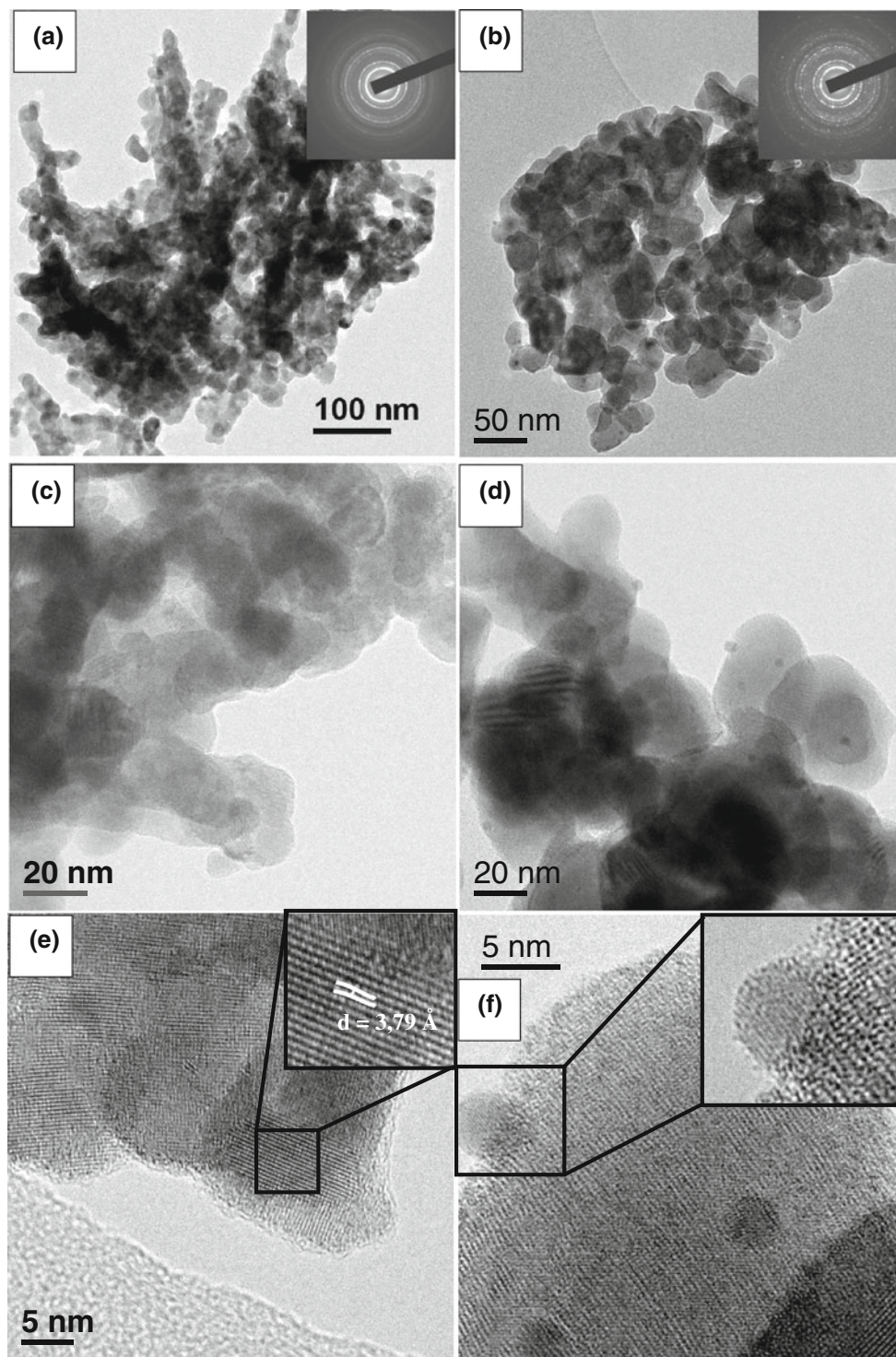
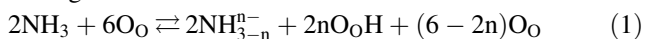


**Fig. 4** TEM and HRTEM images of Cr-doped (a, c, e) and Pt-doped (b, d, f)  $\text{WO}_3$  sol-gel films. *Insets* in figure a, b report the SAED patterns of the Cr and Pt-doped  $\text{WO}_3$  nanomaterials. *Inset* in figure f shows the magnification of a Pt spherical nanoparticle anchored to the  $\text{WO}_3$  surface

groups and  $\text{NH}_3^{n-}$  species ( $n = 1, 2, 3$ ) are produced following reaction 1:



$\text{NH}_3^{n-}$  species successively interact between them leading to the formation of molecular nitrogen

(reaction 2A). Otherwise, they can react with oxygen centers to form nitrogen monoxide (Reaction 2B), which is the favored path in an oxygen-containing atmosphere. Finally,  $\text{NH}_3^{n-}$  species may reduce NO to  $\text{N}_2\text{O}$  by reaction (2C) [30, 31].

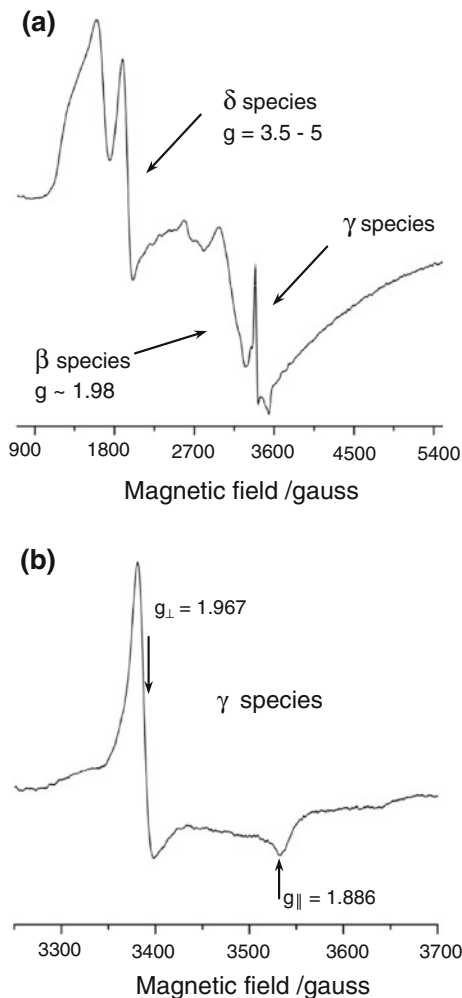
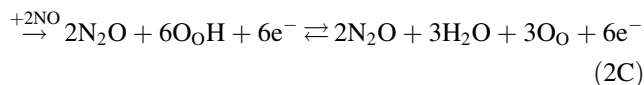
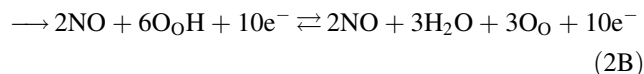
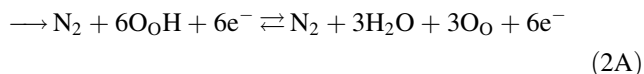
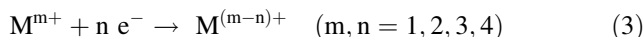


**Fig. 5** EPR spectra recorded at 130 K and  $p < 10^{-2}$  mbar of Cr-doped  $\text{WO}_3$  powders annealed in air (20 mbar) at 250 °C. In large sweep spectra **a** Cr species are labelled as  $\delta$ ,  $\beta$  and  $\gamma$ . **b** Enlarged spectra in the region of the Cr(V) resonances ( $\gamma$  species) and corresponding  $g$  tensor values

All these processes generate electrons and increase the  $\text{WO}_3$  conductance.

In the presence of doping metal, we suggested that the metal centers trap (reaction 3) the electrons derived from reactions (2A–2C), and right hand shift all processes 2A–2C. This allows the production of further electrons, increasing the electrical response [15]:



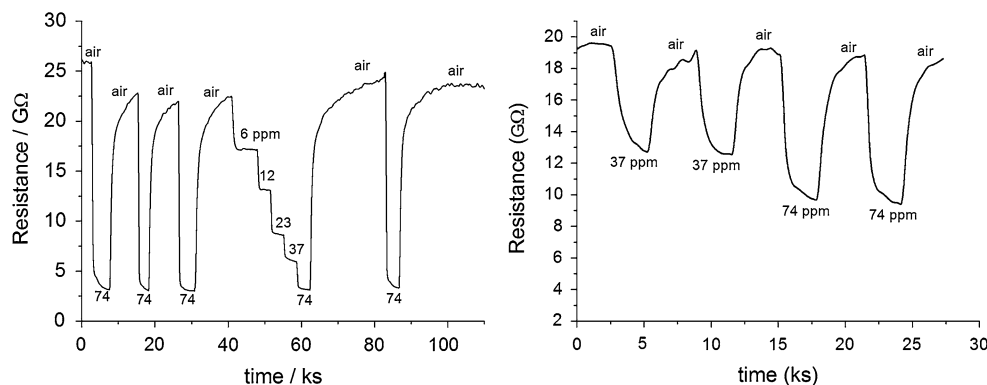
Transition metal doped  $\text{WO}_3$  mesoporous films are in principle expected to combine the effects due to the metal electronic sensitizer with those of the porous morphology, suitable for fast gas diffusion through the sensing layer and easy accessibility to the surface active sites.

The electrical response of doped and undoped  $\text{WO}_3$  films was evaluated by measuring the resistance variation under alternating air and  $\text{NH}_3$ /air flows. Examples of resistance variation at different concentrations of  $\text{NH}_3$ /air mixture for Pt-doped and Cr-doped  $\text{WO}_3$  samples are shown in Fig. 6.

The sensor response was evaluated as  $S = R_{\text{AIR}}/R_{\text{MIX}}$ , where  $R_{\text{AIR}}$  is the resistance under air and  $R_{\text{MIX}}$  is the electrical resistance under  $\text{NH}_3$ /air gas. The variations of the electrical response were taken at different temperatures (200–325 °C) and for different  $\text{NH}_3$  concentrations (6.2–74 ppm) in dry air. Figure 7 reports the electrical responses as a function of the operating temperatures for undoped, Cr-doped, and Pt-doped  $\text{WO}_3$  films under different  $\text{NH}_3$  concentrations.

All samples showed a similar temperature-dependence of the sensitivity, marked by a maximum at 250 °C and by a decrease at the highest temperatures. At each  $\text{NH}_3$

**Fig. 6** Examples of electrical responses at  $T = 300$  °C of (left) Pt-doped and (right) Cr-doped sol-gel  $\text{WO}_3$  films to different concentrations of  $\text{NH}_3$  in synthetic air



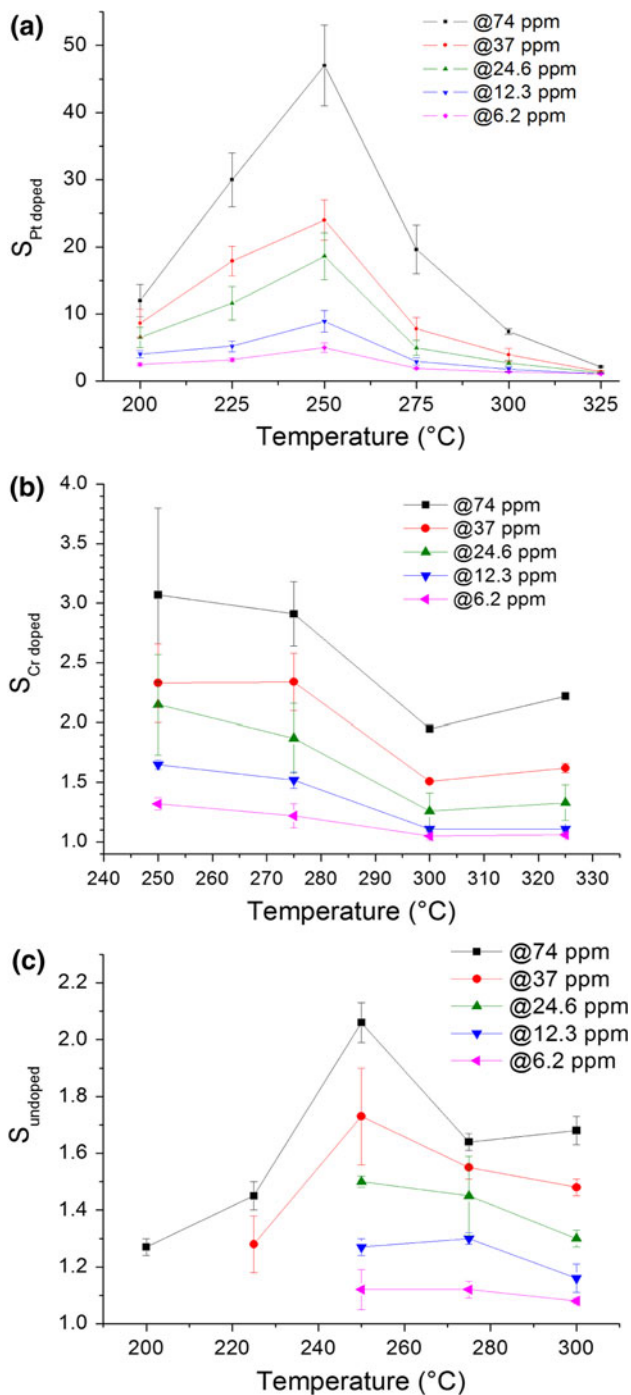


**Fig. 7** Temperature dependence of sensor response of **a** Pt-doped; **b** Cr-doped and **c** pure WO<sub>3</sub> films at different NH<sub>3</sub> concentration in dry air

concentration, Pt-doped samples display higher electrical responses compared to Cr-doped and undoped ones. In particular, Pt-doped WO<sub>3</sub> layers show the best performances at 250 °C under 74 ppm of NH<sub>3</sub> ( $S = 47$ ), with a significant response even at 6.2 ppm ( $S = 5$ ), the lowest

**Table 1** Electrical sensitivity and recovery times detected for Pt-doped WO<sub>3</sub> sol–gel films

Temperature (°C)	$S = R_{AIR}/R_{MIX}$ under NH <sub>3</sub> (74 ppm)/air	$S = R_{AIR}/R_{MIX}$ under NH <sub>3</sub> (6.2 ppm)/air	Recovery times from NH <sub>3</sub> (74 ppm)/air
200	12.0	2.5	>20 h
225	30	3.2	≈ 10 h
250	47	5.0	≈ 5 h
275	19.6	1.9	≈ 2 h
300	7.4	1.4	≈ 50 min
325	2.13	1.1	≈ 10 min

NH<sub>3</sub> concentration. The electrical response for the Pt-doped WO<sub>3</sub> films and the corresponding recovery times at the highest ammonia concentration are reported in Table 1. It is interesting to note that increasing the temperature till 300–325 °C, Pt-doped films display relatively short recovery times (~50–10 min), which become significantly higher when the temperature is below 250 °C (see Table 1).

The maximum shaped trend of the electrical sensitivity is probably caused by a balance between two opposite effects. In fact, upon heating, ammonia reactions (2A–2C) at the oxide surface become faster and the response increases. On the other hand, NO, a side product of ammonia oxidation (reaction 2B), can easily react with O<sub>2</sub> to produce NO<sub>2</sub>, which acts as oxidizing agent and increases the layer resistance. At high temperature the NO<sub>2</sub> oxidizing effect succeeds, while at a low temperature, being the conversion of NH<sub>3</sub> to NO less favored, the NH<sub>3</sub> reducing effect prevails [32].

In order to better describe the sensitivity towards NH<sub>3</sub>, the electrical response of all layers is reported as a function of NH<sub>3</sub> concentration at several operating temperatures (Fig. 8). At each temperature, layers generally easily detect the different concentrations of ammonia.

Pt-doped WO<sub>3</sub> layers showed the best performances at all temperatures. The reason for the higher electrical sensitivity of Pt-doped WO<sub>3</sub>, with respect to Cr-doped, cannot be attributed only to higher amounts of electrons trapped by positive Pt center expected from the sensitization mechanism (3). Instead it can be also related to the presence of the Pt nanoparticles, revealed by HRTEM analysis. Following a recent literature suggestion, these finely distributed Pt particles may act as catalysts of the interaction between ammonia and O<sub>o</sub> centers [33], decreasing the activation barrier in the reaction 1 and promoting the dissociation of the N–H bond.

Even if much lower than Pt-doped WO<sub>3</sub> sensors, the electrical response of Cr-doped WO<sub>3</sub> layers is always higher than pure WO<sub>3</sub>, in particular at 275 °C (onset on Fig. 8a). This confirms that the doping with chromium



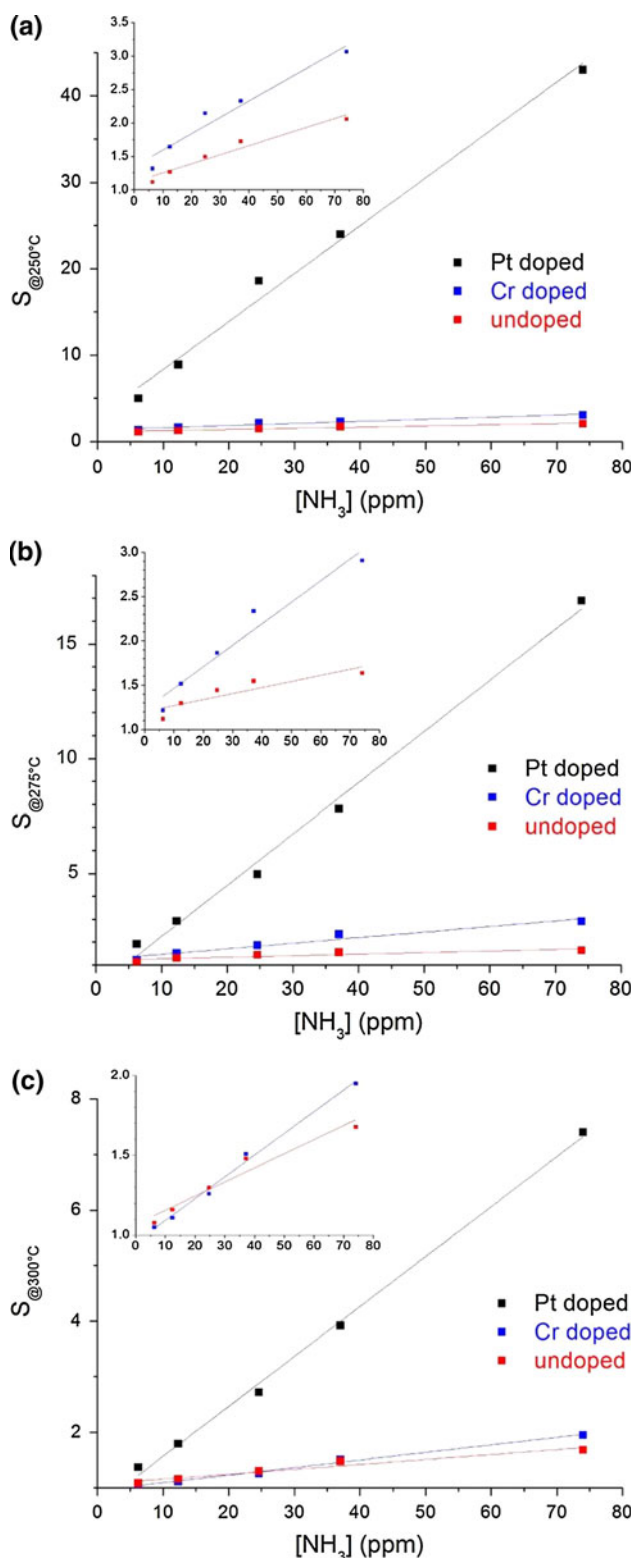


**Fig. 8** Comparison among the electrical responses of Pt-doped, Cr-doped and pure  $\text{WO}_3$  films as a function of ammonia concentration in dry air at different temperatures: **a** 250 °C, **b** 275 °C, **c** 300 °C. *Insets* in **a**, **b** and **c** highlight the differences between undoped and Cr-doped sensor responses which are difficult to appreciate in the full scale

anyhow improves the electrical response of  $\text{WO}_3$  films. In fact, Cr(III) and Cr(V) centers detected by EPR, should accept the electrons injected by  $\text{NH}_3$  (following reaction 3) decreasing their positive oxidation state and increasing the overall sensitivity.

The overall results suggest that the combination between mesoporous architecture and metal doping can really promote the electrical response of  $\text{WO}_3$  toward ammonia.

However, it appears an open problem whether the morphology is less or more effective than the doping metal in influencing the electrical properties of metal oxide gas sensors. In fact, several investigations report about the sensing performance of oxides with different morphologies [26, 27, 30–32], mainly in the case of nanostructures, but only very few consider the comparison among transition metal-doped oxides having the same morphology [34]. Interestingly in the case of Cr-doped  $\text{WO}_3$ , it has been reported that the metal doping is able to quench the electrical differences due to two different nanostructures, and the electrical behavior is fully influenced by the dopant metal [34]. The results obtained in the present study for Cr-doped  $\text{WO}_3$  thin films seem therefore in line with this behavior: the higher electrical response induced by Pt than by Cr doping  $\text{WO}_3$  with the same nanostructure can be mainly attributed to the different ability of two metals to undergo reduction. Thus, mechanistic effects related to chemisorption and gas diffusion in mesoporous oxide appear less determinant than the electronic differences between the two examined doping metals.

#### 4 Conclusions

A fast one-step sol–gel procedure, based on the use of triblock copolymer as templating agent, was successfully applied to synthesize both undoped and Cr or Pt-doped  $\text{WO}_3$  mesoporous thin films, to be employed as ammonia gas sensors.

The obtained films were constituted by aggregates of interconnected  $\text{WO}_3$  nanocrystals (20–50 nm) separated by mesopores with dimensions ranging between 5 and 15 nm. The doping metals, Pt and Cr, resulted differently hosted in the  $\text{WO}_3$  mesoporous matrix. Chromium is homogeneously dispersed in the oxide matrix, mainly as Cr(III) and Cr(V) centers, as revealed by EPR spectroscopy; instead platinum segregated as Pt (0) nanoparticles (4 nm) mainly included inside  $\text{WO}_3$  nanocrystals. This was related to the expected easier reducibility of the Pt centers compared to the Cr ones in the presence of triblock copolymer template, and to the Pt aggregation into clusters moving through the channels of the  $\text{WO}_3$  open perovskite structure.

The  $\text{WO}_3$  semiconductor layers containing Pt nanoclusters revealed, upon exposure to  $\text{NH}_3$ , remarkable electrical responses, much higher than Cr-doped and undoped layers, particularly at low ammonia concentration (6.2 ppm). This behavior was attributed to the presence of Pt nanoparticles segregated inside the semiconductor matrix, which act as catalysts of the N–H bond cleavage, decreasing the activation barrier in the ammonia dissociation. This probably makes the major difference with the simple electron capture performed by the oxidized doping centers. Thus, the electrical properties of Pt and Cr-doped  $\text{WO}_3$  thin films, can be mainly related to the different reducibility of the dopants.

The role of the mesoporous structure in influencing the chemisorption and the gas diffusion in the  $\text{WO}_3$  matrix appears less decisive than the electronic differences between the two examined metals.

The overall results support the validity of this synthesis method to supply promising nanomaterials for the detection of ammonia even at low concentration.

**Acknowledgments** The Milano group gratefully acknowledges the financial support of the Cariplo Foundation of Milano. The authors also personally thank Davide Fumagalli for his support in the experimental part.

## References

- Göpel W, Hesse J, Zemel JN (1991) *Sensors. A comprehensive survey, vol 2: Chemical and biochemical sensors (Parts 1 and 2)*. VCH Weinheim, New York
- Barsan SN, Bauer M, Weimar U (2001) *Sens Actuators B* 73: 1–26
- Göpel W, Hesse J, Zemel JN, Meixner H, Jones R (1995) *Sensors. A comprehensive survey, vol 8*. VCH Weinheim, New York
- Moseley PT, Tofield BC (1987) *Solid-state gas sensors*. Hilger, Bristol/Philadelphia
- Sberveglieri G (1992) *Gas sensors: principles, operation and developments*. Kluwer, Boston
- Mandelis A, Christofides C (1993) *Physics, chemistry and technology of solid state gas sensor devices*. Wiley, New York
- Cui Y, Wie Q, Park H, Lieber CM (2001) *Science* 293: 1289–1292
- Xia Y, Yang P, Sun Y, Wu Y, Mayers B, Gates B, Yin Y, Kim F, Yan H (2003) *Adv Mater* 15:353–389
- Lee JH (2009) *Sens Actuators B* 140:319–336
- Scott RWJ, Yang SM, Coombs N, Williams DE, Ozin GA (2003) *Adv Funct Mater* 13:225–231
- Acciarri M, Barberini R, Canevali C, Mari CM, Mattoni M, Morazzoni F, Nodari L, Polizzi S, Ruffo R, Russo U, Sala M, Scotti R (2005) *Chem Mater* 17:6167–6171
- Sasahara K, Hyodo T, Shimizu Y, Egashira M (2004) *J Eur Ceram Soc* 24:1961–1967
- Wang H, Liang J, Fan H, Xi B, Zhang M, Xiong S, Zhu Y, Qian Y (2008) *J Solid State Chem* 181:122–129
- Firooz AA, Mahjoub AR, Khodadadi AA (2009) *Sens Actuators B* 141:89–96
- D'Arienzo M, Armelao L, Cacciamani A, Mari CM, Polizzi S, Ruffo R, Scotti R, Testino A, Wahba L, Morazzoni F (2010) *Chem Mater* 22:4083–4089
- Choi WK, Song SK, Cho JS, Yoon YS, Choi D, Jung HJ, Koh SK (1997) *Sens Actuators B* 40:21–27
- Canevali C, Chiodini C, Morazzoni F, Scotti R, Bianchi CL (1997) *J Mater Chem* 7:997–1002
- Canevali C, Mari CM, Mattoni M, Morazzoni F, Nodari L, Ruffo R, Russo U, Scotti R (2005) *J Phys Chem B* 109:7195–7202
- Niederberger M, Garnweitner G (2006) *Chem Eur J* 12: 7282–7302
- Polleux J, Gurlo A, Barsan N, Weimar U, Antonietti M, Niederberger M (2006) *Angew Chem Int Ed* 45:261–265
- Yang P, Zhao D, Margolese DI, Chmelka BF, Stucky GD (1998) *Nature* 396:152–155
- Bailey FE, Koleske JV (1990) *Alkylene oxides and their polymers*. Marcel Dekker, New York
- Pokhrel S, Simion CE, Teodorescu VS, Barsan N, Weimar U (2009) *Adv Funct Mater* 19:1767–1774
- Xu C, Tamaki J, Miura N, Yamazoe N (1991) *Sens Actuators B* 3:147–155
- Simon I, Barsan N, Bauer M, Weimar U (2001) *Sens Actuators B* 73:1–26
- Epifani M, Andreu T, Magaña CR, Díaz R, Arbiol J, Siciliano P, Morante JR (2010) *Sens Actuators B* 148:200–206
- Epifani M, Andreu T, Arbiol J, Diaz R, Siciliano P, Morante JR (2009) *Chem Mater* 21:5215–5221
- Brunauer S, Emmet PH, Teller E (1938) *J Am Chem Soc* 60:309–319
- Barret EP, Joyner LG, Halenda PP (1951) *J Am Chem Soc* 73:373–380
- Jimenez I, Centeno MA, Scotti R, Morazzoni F, Arbiol J, Cornet A, Morante JR (2004) *J Mater Chem* 14:2412–2420
- Morazzoni F, Scotti R, Origoni L, D'Arienzo M, Jimenez I, Cornet A, Morante JR (2007) *Catalysis Today* 126:169–176
- Zamani C, Casals O, Andreu T, Morante JR, Romano-Rodriguez A (2009) *Sens Actuators B* 140:557–562
- Mudiyanselage K, Trenary M, Meyer RJ (2007) *J Phys Chem C* 111:7127–7136
- Rossinyol E, Prim A, Pellicer E, Arbiol J, Hernández-Ramírez F, Peiró F, Cornet A, Morante JR, Solovyov LA, Tian B, Bo T, Zhao D (2007) *Adv Funct Mater* 17:1801–1806